

# N<sub>2</sub> solar activation: ammonia as a hydrogen vector for energy storage

Lorenzo Rizzato,  \*<sup>a</sup> Jonathan Cavazzani,  <sup>a</sup> Andrea Osti  <sup>a</sup> and Antonella Glisenti  <sup>ab</sup>

Received 7th November 2022, Accepted 5th December 2022

DOI: 10.1039/d2fd00147k

From the plethora of energy-intensive synthetic processes, ammonia production has a particularly negative impact due to the high-energy consumption caused by the Haber–Bosch process and the high greenhouse gas (GHG) emission rate. Thus, new and effective ways to activate N<sub>2</sub> and synthesise NH<sub>3</sub> are crucial to reduce production costs and the anthropogenic footprint derived from the current harsh reaction conditions. In this study, two-dimensional materials have been employed in the photoactivation of nitrogen in an aqueous medium; M<sup>I</sup>(<sup>II</sup>)M<sup>II</sup>(<sup>III</sup>) (with M<sup>I</sup> = Cu or CuNi, and M<sup>II</sup> = Cr or Al) layered double hydroxides have been synthesised using a simple, economical and scalable co-precipitation/filtration method. The structural and functional properties were systematically investigated by XRD, SEM, TPR and BET; the results indicate that the prepared LDHs were successfully synthesised, possess high surface areas and, in the case of CuAl LDH, the material showed a nanoplate-like structure, thus confirming the two-dimensional nature of this class of catalyst. The N<sub>2</sub> fixation performances were evaluated using a scalable, cost-effective and low-energy-consuming setup: from the catalytic tests, a NH<sub>3</sub> production rate of 99 μmol g<sup>-1</sup> h<sup>-1</sup> was observed, demonstrating LDHs' high potential and the scalability of the overall process.

## Introduction

As one of the most synthesised molecules in the world, ammonia serves as a useful feedstock in several industrial fields, from the preparation of reactive nitrogen-containing compounds to its important role in agriculture.<sup>1–3</sup> Moreover, the favourable thermodynamics of the cracking reaction that forms N<sub>2</sub> and H<sub>2</sub> make NH<sub>3</sub> a promising energy carrier,<sup>4</sup> possessing the ability to release hydrogen and therefore proposing itself as a candidate against carbon-based fuels.<sup>5</sup> Currently, ammonia synthesis is mainly carried out *via* the Haber–Bosch process,<sup>6</sup> employing N<sub>2</sub> and H<sub>2</sub>; however, harsh conditions are required to effectively

<sup>a</sup>Department of Chemical Sciences, University of Padova, Via F. Marzolo 1, 35131, Padova, Italy. E-mail: lorenzo.rizzato.1@phd.unipd.it

<sup>b</sup>ICMATE – Department of Chemical Sciences, University of Padova, Via F. Marzolo 1, 35131, Padova, Italy



activate the dissociation of dinitrogen<sup>7</sup> and hydrogen is often produced through steam reforming, therefore depending on fossil fuels and generating CO<sub>2</sub>.<sup>8,9</sup> In fact, ammonia synthesis processes are responsible for 1% of the global energy consumption and for 3% of carbon dioxide emissions.<sup>10</sup> Thus, new synthetic paths are currently being studied to produce ammonia under milder conditions, lowering the working temperature and pressure, and finding new strategies to effectively break the strong dinitrogen triple bond.<sup>11–13</sup> Activation is the major bottleneck of the entire process; therefore, new materials able to effectively adsorb the dinitrogen molecule and activate the hydrogenation reaction are required to obtain sustainable and green ammonia.<sup>14,15</sup>

Understanding the nitrogen reduction reaction (NRR) and its kinetics is crucial to design an active catalyst able to achieve nitrogen fixation. In general, associative and dissociative pathways, with various reaction intermediates, mainly compose the nitrogen fixation process.<sup>16</sup> In the dissociative pathway, the triple bond is activated to generate two separated adsorbed nitrogen atoms, which separately react with hydrogen to form NH<sub>3</sub> and are subsequently desorbed from the surface; however, the high bonding energy (9.79 eV)<sup>17</sup> of the triple bond makes the dissociative catalytic activation difficult under mild conditions. Contrarily, the associative pathway involves the adsorption of the dinitrogen molecule onto the catalyst surface and the resulting sequential protonation of the two N atoms, thus reducing the required energy to activate the N<sub>2</sub> molecule and favouring the formation of ammonia. To address the sluggish NRR kinetics under mild conditions, alternative energy vectors with respect to heat can be considered, as photons or electrons.<sup>18–20</sup> Indeed, photocatalytic and electrocatalytic approaches have drawn much attention, due to their ability to convey the required energy for the reaction without raising the temperature and therefore making the reaction more sustainable.<sup>21,22</sup>

As for the photocatalytic nitrogen reduction, the activation of the molecule requires the excitation of electron/hole pairs by means of light absorption and subsequent stimulation of the catalyst.<sup>23</sup> The photogenerated electrons and holes are then employed in the redox reaction, involving nitrogen and a reducing agent, such as hydrogen or water. As this process requires both the charge transfer between the material and the active site, and the electron donation from the catalyst to the nitrogen molecule, it is considered the rate determining step of the catalytic reaction.<sup>24</sup> To address this problem, band gap engineering and defect control are required to design a proper catalyst; moreover, suitable conduction and valence band positions and selective active sites are crucial to suppress the hydrogen evolution reaction and therefore maximise the quantity of ammonia produced.<sup>25,26</sup> In a similar way, electrocatalytic ammonia synthesis involves charge and mass transfer to conduct the dinitrogen conversion in the presence of an electric field.<sup>27</sup> Considering the cathodic processes, of which the nitrogen reduction reaction mainly consists, good N<sub>2</sub> adsorption and selectivity are needed to suppress parasitic reactions, thus increasing the ammonia yield.<sup>28</sup> However, low performances are obtained at atmospheric conditions to date, thus making the photocatalytic approach more feasible for ammonia synthesis.<sup>29</sup>

Different catalyst design approaches have been reported so far, including biomimetic metal complexes,<sup>30</sup> surface-decorated oxides with plasmonic nanoparticles<sup>31</sup> and bidimensional materials.<sup>32</sup> Due to their low cost, great tunability and good performances, ultrathin nanosheets have drawn much attention to



date. Since the discovery of graphene, several types of layered structures have been developed,<sup>32</sup> namely, transition metal chalcogenides, graphitic carbon nitride, MXenes and layered double hydroxides, which represent the state of the art of 2D nanomaterials for catalytic conversion.<sup>17</sup> All of these materials are characterised by good band-gap tunability and good light absorption, thus leading to the design of efficient photocatalysts in the visible range. 2D chalcogenides intrinsically possess a small band gap (2–3 eV) and good charge transport properties, making them good candidates for photocatalytic N<sub>2</sub> fixation; however, photocorrosion and good synthetic methods still need to be addressed to effectively make chalcogenides a feasible choice.<sup>33</sup> Graphitic carbon nitride (g-C<sub>3</sub>N<sub>4</sub>) possesses a compatible band gap, a high concentration of surface-active sites and an interesting electronic structure for nitrogen fixation.<sup>34</sup> However, its fast charge-recombination rate makes this material difficult to use in photocatalysis in its bare structure.<sup>35</sup> To overcome this problem and therefore enhance the performance, surface and defect engineering have to be employed. The electronic structure of MXenes greatly enhances nitrogen adsorption, thus effectively activating the N<sub>2</sub> fixation reaction,<sup>36,37</sup> however, these materials cannot be directly employed in photocatalysis due to their metallic properties. Thus, different kind of structures, such as heterostructures or Z-scheme catalysts that incorporate MXenes, are needed to exploit their photocatalytic properties.

From the plethora of possible active 2D catalysts for ammonia synthesis, nanostructured layered double hydroxides (LDHs) are a promising category of semiconductors, possessing interesting properties.<sup>38,39</sup> The presence of under-coordinated metal sites and the great surface area potentially enhance the N<sub>2</sub> adsorption and activation. Moreover, surface defect control and engineering enhance the catalytic activity by tuning the electronic and adsorption properties.<sup>40</sup> Layered double hydroxides are generally characterised by a brucite-like structure with intercalated anions that balance the positively charged surface.<sup>22</sup> As different metallic cations can be employed in LDHs, the electronic structure can be finely tuned to design an efficient catalyst for nitrogen fixation.<sup>41–43</sup>

Herein, we report the design of Cu and Ni-based layered double hydroxides for dinitrogen fixation and ammonia production, along with a simple and environmentally friendly synthetic method. In this work, chromium- and aluminium-based LDHs were chosen for their good light absorption in the visible region,<sup>44,45</sup> along with their ability to form layered structures in a simple and effective way; moreover, the ability of Cr and Al species to interact with N<sub>2</sub> is crucial for the purpose of this work.<sup>46,47</sup> In addition, the insertion of copper as the LDH's divalent metal can significantly improve the catalytic activity, as the presence of a Jahn–Teller distortion was proven to play an important role in the defect concentration enhancement and in the electronic structure modification. Finally, partial copper substitution with nickel atoms could further improve the catalytic performances of LDHs, as they can modify the electronic structure of the catalyst, lowering the N<sub>2</sub> adsorption energy and enhancing the NH<sub>3</sub> production rate, as previously demonstrated.<sup>48</sup> In this work, LDHs' photoactivated N<sub>2</sub> fixation ability is investigated by means of a cost-effective, scalable and low-energy-intensity system, comprising a commercial 100 W visible-light LED lamp; indeed, the possibility of producing ammonia using a low impacting technology is crucial to achieve a good compromise between catalytic performance and



reaction conditions, and thus overcome the limitations of the Haber–Bosch  $\text{NH}_3$  production process.

## Results and discussion

The comparison of the diffractograms allows us to observe that all samples, apart from CuAl, show similar behaviour. The diffraction data obtained from CuCr are similar to those reported in the literature for samples obtained with different synthetic methods,<sup>49–51</sup> thus suggesting that the procedure used for this work is proven to be effective to obtain layered double hydroxides, with the advantages of being simple, economical, and scalable. Indeed, the methods reported so far use hydrothermal reactors or co-precipitation procedures with non-aqueous solvents, thus making the scale-up difficult in the first case, and more expensive and less sustainable for the latter case.

From literature data, the XRD patterns observed for CuCr, CuNiCr and CuNiAl match the JCPDS no. 37-0630 (hydrotalcite structure), with reflections assigned to (003), (006) and (009) diffraction planes along with the (110) facet at  $2\theta = 60.4^\circ$ , as can be seen in Fig. 1.<sup>52</sup> Moreover, a hexagonal structure with rhombohedral symmetry can be derived from the diffraction pattern.<sup>53</sup> Comparing the crystallite dimensions calculated from the Scherrer equation, it was found that, based on the most intense peak, the crystallites of CuCr, CuNiCr, and CuNiAl should have dimensions of  $<2$  nm, while CuAl should possess  $\sim 30$  nm crystallites. A summary of the aforementioned calculated data is presented in Table 1. From the comparison between the CuCr and CuNiCr samples, a shift towards higher angles of  $2\theta = 0.9^\circ$  can be observed, thus indicating a compression of the unit cell, and therefore meaning that Ni atoms were successfully integrated in the structure. In

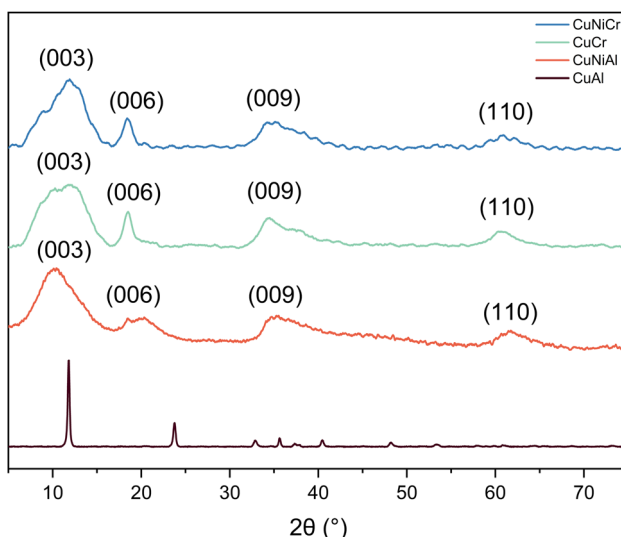


**Fig. 1** XRD patterns of Cr- and Al-containing samples. For CuCr, CuNiCr and CuNiAl, a hydrotalcite-type structure can be identified, while, for CuAl, no defined structure was found.



Table 1 Average crystallite dimensions calculated using the Scherrer equation

Sample	Crystallites' average dimension (nm)
CuCr	1.42
CuNiCr	1.42
CuAl	27.31
CuNiAl	1.24

addition, the absence of CuO and NiO reflections seems to suggest a complete incorporation of nickel and copper atoms in the hydrotalcite-like structure. A different pattern can be observed for CuAl: indeed, CuAl resulted in sharper and more intense reflections, centred at different angles with respect to the other LDHs. Based on previous literature work, no match was found for this type of diffractogram; however, no detectable impurities of Al(OH)<sub>3</sub>, or the two reflections at  $2\theta = 32^\circ$  and  $2\theta = 39^\circ$  that can be ascribed to a copper oxide phase,<sup>54</sup> can be derived from the pattern analysis. Indeed, the absence of evidence for this type of structure made the identification of the phase difficult and deeper analyses are needed. Diffraction pattern differences between this material and the CuNiAl LDH could be caused by a different morphology or facet exposition, which could significantly modify the contribution in the XRD pattern.

To further confirm the hypothesis that emerged from analysis of the XRD patterns, SEM images were taken, and the morphology of the different catalysts was observed (Fig. 2). Scanning electron micrographs of the as-prepared catalysts show different structures: for CuCr, CuNiAl and CuNiCr, the morphology seems to be similar, with the presence of aggregates that suggest a strong interaction

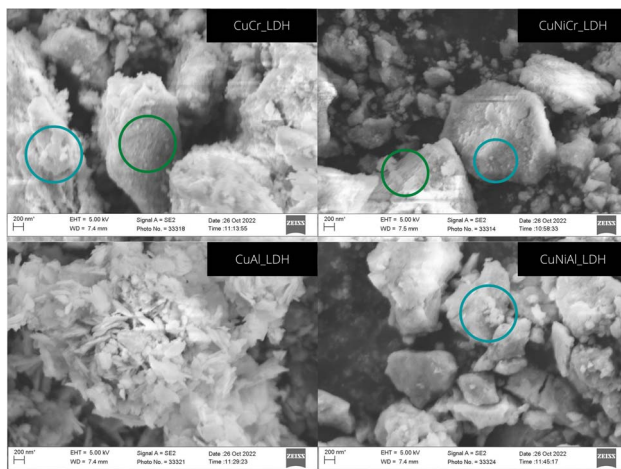


Fig. 2 SEM images of the synthesised LDHs. The nanostructured morphology of CuAl can be easily observed, while little signs of delamination are present in the other materials; indeed, denser structures in the form of aggregates can be spotted in the CuCr, CuNiCr and CuNiAl materials. Signs of delamination are highlighted with green circles, while blue circles indicate particle agglomeration.



between the nanosheets. Indeed, the particles observed seem to be formed by smaller structures stacked randomly to form large aggregates; additionally, signs of particle delamination and sheet aggregation can be spotted at high magnification. Examining in more detail, the Ni-containing LDHs seem to possess denser structures and aggregates with respect to the CuCr morphology, which seems to be more delaminated and formed by smaller aggregates. Differently, CuAl possesses a nanoflake-like morphology, with plate aggregates and a lateral dimension of 10 nm. The different morphology could explain the divergence in the XRD pattern between this material and the other synthesised LDHs. Moreover, the morphological observations confirm the presence of small crystallites in CuCr, CuNiCr and CuNiAl, and of larger particles for CuAl, as predicted with the Scherrer equation.

Another important parameter that greatly influences the catalytic performance is the specific surface area (SSA); indeed, active-site exposition is crucial to ensure good interaction with the reactants. SSA measurements through BET calculation denoted a high surface area for all samples, with a hysteresis curve typical of type IV materials.<sup>55</sup> Additionally, pore volume analysis using BJH adsorption curves indicated the presence of a high concentration of mesopores with a radius  $<10$  nm, thus confirming the mesoporous nature of the prepared samples. The differences in specific surface area could be affected either by composition or by different interactions between particles, thus causing the particles to aggregate differently according to the catalyst structure. Indeed, the CuNiAl sample shows a higher surface area with respect to the CuCr and CuAl samples, suggesting that the insertion of a second divalent metal could result in a higher concentration of defect sites and, therefore, in an improved number of open pores in the system. From SSA measurements, CuNiAl resulted in a surface area of  $298.8\text{ m}^2\text{ g}^{-1}$ , outperforming the other samples by almost one degree of magnitude. This behaviour could be caused by a lower intermolecular interaction between different nanosheets, thus promoting the exposition of facets and the consequent improvement in the surface area.<sup>56</sup> As can be seen in Table 2, the CuNiAl LDH presents smaller pores, thus indicating an almost-microporous material and confirming the low-interaction hypothesis.

Comparing the BET measurement results (Fig. 3), an inverse proportional behaviour between the specific surface area and the mean pore size seems to emerge; indeed, CuNiAl possesses a high SSA and small pores, while CuCr shows bigger pores but a lower surface area. This evidence further supports the presence of more spaced and less interacting nanosheets in CuNiAl with respect to the other layered structures.

From temperature programmed reduction measurements, a strong signal from 200 to 300 °C can be observed in all the samples (Fig. 4); this evidence can be

**Table 2** Specific surface area and mean pore size of all synthesised LDHs

Sample	Specific surface area ( $\text{m}^2\text{ g}^{-1}$ )	Mean pore size (nm)
CuCr	55.21	10.71
CuNiCr	31.94	7.23
CuAl	84.62	9.68
CuNiAl	298.8	3.06



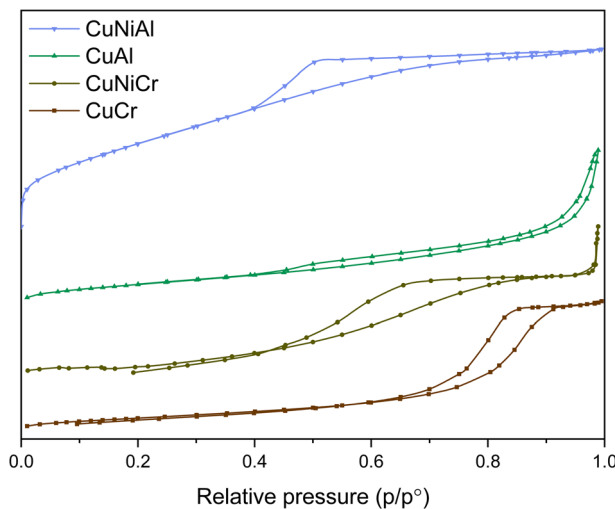


Fig. 3 BET isotherms for each synthesised LDH. Typical type IV curves can be observed for all the samples, confirming the mesoporous nature of the catalysts. Each BET curve is shifted by  $2 \text{ mmol g}^{-1}$ .

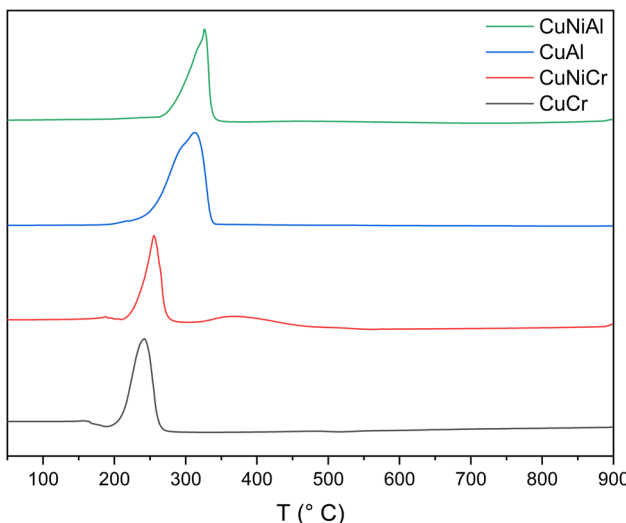


Fig. 4 Temperature programmed reduction measurements for the synthesised LDHs.

correlated with the presence of Cu species.<sup>57</sup> However, the peak shapes are rather complex, thus leading to the hypothesis of at least two reduction steps ( $\text{Cu}^{2+} \rightarrow \text{Cu}^+$  and  $\text{Cu}^+ \rightarrow \text{Cu}^0$ ); the influence of a different chemical environment surrounding Cu atoms cannot be excluded.<sup>58</sup>

In general, when the trivalent metal is Cr, the reduction peaks are shifted  $\sim 60$   $^\circ\text{C}$  towards lower temperatures with respect to Al-containing structures. This can be explained by a more effective stabilization effect of Al with respect to reduction.

Indeed, the ability of aluminium atoms to stabilise an oxide structure was observed also in brownmillerites. This is confirmed by the comparison between the curves of the Ni-containing LHD. The presence of Ni in the structure resulted in the emergence of a new peak, at around 368 °C (due to the reduction of Ni), only in the sample without aluminium. The CuCr TPR signal presented a single peak at 220 °C, corresponding to the reduction of Cu species in the layered hydroxide and a second, more intense peak at 242 °C.<sup>49</sup> Adding Ni as a second divalent metal results in the presence of an additional signal in the Cu reduction zone and a general shifting towards higher temperatures, thus leading to the conclusion that the structure of the hydroxide could have been altered, thus changing the interaction between the Cu atoms and the surrounding LDH structure. Similarly, CuAl presents a different signal shape compared to the same peak of the Ni-containing counterpart; the former can be deconvoluted into two different peaks, one at 291 °C and the other at 316 °C, suggesting two different reduction processes for Cu. The peak at 316 °C could be related to the reduction of Cu<sup>2+</sup> to Cu<sup>0</sup> of the CuO impurities found in the X-ray diffraction pattern, while a more reducible copper species could be responsible for the lower temperature signal. The most accredited possibility for the signal at 291 °C seems to be the reduction of Cu atoms in the structure of the nanosheet, as reported in the literature.<sup>52</sup> As regards the CuNiAl sample, the reduction signal of Cu mimics the behaviour of the Cr-containing counterpart, resulting in a 10 °C shifting and in the emergence of a new peak at 318 °C. A broad and weak signal can be observed between 370 °C and 550 °C, indicating the presence of Ni species in the structure.

As regards the catalytic performance of the prepared layered double hydroxides, all the materials were found to be active for light-induced dinitrogen fixation. The NH<sub>3</sub> production rates are reported in Fig. 5; CuNiAl LDH converted nitrogen at 99 μmol g<sup>-1</sup> h<sup>-1</sup>, followed by CuNiCr (92 μmol g<sup>-1</sup> h<sup>-1</sup>), CuCr (80 μmol g<sup>-1</sup> h<sup>-1</sup>) and CuAl (40 μmol g<sup>-1</sup> h<sup>-1</sup>). In general, the Cr-based LDHs performed better than CuAl and CuNiAl, probably due to the better light absorption properties of Cr atoms in the visible region. Indeed, the Al<sup>3+</sup> absorption maximum is

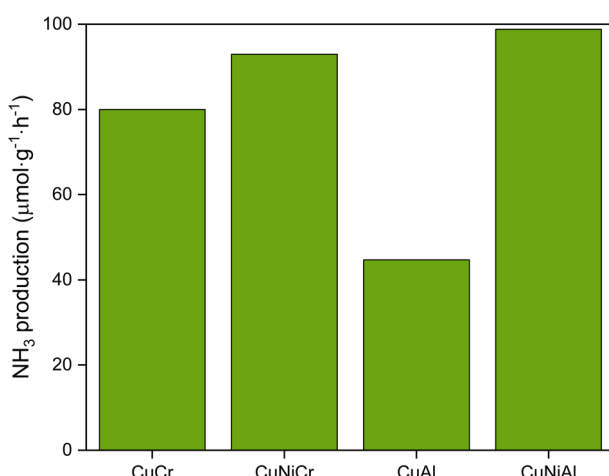


Fig. 5 NH<sub>3</sub> production of different LDHs; Ni-containing samples resulted in an improvement of the N<sub>2</sub> conversion.



shifted towards the UV region,<sup>59</sup> thus not taking advantage of the full LED emission spectrum. Additionally, the bigger crystallites observed for CuAl may influence the activity by lowering the surface area, and therefore the number of catalytic sites. As can be seen, the insertion of Ni in the nanosheets structure results in a great improvement of catalytic performance, with CuNiCr and CuNiAl producing 1.2 and 2.2 times more ammonia than CuCr and CuCr, respectively. The role of Ni in the improvement of the catalyst activity has to be further explored to fully understand the activation mechanism of the reaction. However, based on previous literature work, the addition of a second divalent metal could produce new defect sites, modifying the electronic structure and adding new energy levels, resulting in a more effective band structure towards the N<sub>2</sub> photofixation reaction. Another possible explanation of the activity enhancement with Ni-containing LDHs could be the catalytic role of Ni in the N<sub>2</sub> photofixation reaction; in this case, Ni atoms could provide new active sites to the catalyst, thus enhancing the performance of the material.<sup>60</sup> Ni atoms could also contribute to the reaction by adsorbing H<sub>2</sub>O on the surface, and therefore increasing the probability of effectual N–H interactions, thanks to their hydrogen adsorption properties.<sup>61</sup> Comparing the NH<sub>3</sub> production rate over surface area ratios of the synthesised catalysts (Table 3), a clear trend can be observed: CuCr performed 2.7 times better than CuAl, and CuNiCr produced 8.2 times more NH<sub>3</sub> with respect to CuNiAl. As mentioned before, the catalytic activities of the LDHs with Ni embedded in the structure show better performances compared with CuCr and CuAl, thus confirming that Ni species play a significant role in the overall reaction. It is worth noting that the CuNiCr LDH produced a decent quantity of NH<sub>3</sub>, despite its low surface area; thus, improvement with this material is expected with a higher surface area. A behaviour similar to the one exhibited by Cr-based structures is found in Al-based layered hydroxides. The small concentration of NH<sub>3</sub> found for CuAl could be due to the acidic chemical environment during the reaction; indeed, the slightly acidic conditions of deionized water could have caused the release of Al<sup>3+</sup> species, with subsequent damaging of the layered double hydroxide structure.

As photocatalytic N<sub>2</sub> fixation using layered double hydroxides is relatively new and little explored, few results for comparison were found in the literature. Comparing these results with previously reported active catalysts, good N<sub>2</sub> fixation properties were obtained from the materials here reported. The CuCr sample was compared with the same material reported previously and with other reference LDHs; the synthesised CuCr produced 2 times more NH<sub>3</sub> with respect to the same material synthesised by Zhao *et al.*<sup>22</sup> and showed better performance compared with other LDHs, such as CuAlZn (35  $\mu\text{mol g}^{-1} \text{h}^{-1}$ )<sup>21</sup> or

**Table 3** NH<sub>3</sub> production over specific surface area ratio

Sample name	NH <sub>3</sub> production/SSA ( $\mu\text{mol m}^{-2} \text{h}^{-1}$ )
CuCr	1.45
CuAl	0.53
CuNiCr	2.91
CuNiAl	0.33



ZnCr ( $60 \mu\text{mol g}^{-1} \text{ h}^{-1}$ ),<sup>62</sup> denoting a positive contribution of copper atoms with respect to Zn species. Moreover, exploring different types of 2D materials, the catalytic  $\text{NH}_3$  production of CuNiAl is comparable with that of a BiOBr nanosheets ( $104 \mu\text{mol g}^{-1} \text{ h}^{-1}$ ) catalyst,<sup>58</sup> though CuNiAl is simpler and more economical to prepare. The LDHs showed better performances with respect to 2D  $\text{TiO}_2$  nanosheets loaded with different transition metals,<sup>63</sup> resulting in an improvement of one order of magnitude. Finally, the catalysts here reported showed better performances with respect to other inorganic catalysts containing noble metals, such as Au/ $\text{TiO}_2$ -OV ( $74 \mu\text{mol g}^{-1} \text{ h}^{-1}$ ),<sup>64</sup> indicating that LDHs could become a competitive material and assure a sustainable future with the use of non-critical raw materials. If compared with graphitic carbon nitride, a clear difference in the performance can be seen, as  $\text{g-C}_3\text{N}_4$  performs 10 times better than layered double hydroxides;<sup>65</sup> this could be due to the lack of research on LDHs as possible catalysts for  $\text{NH}_3$  synthesis from  $\text{N}_2$ , thus not gaining information about the material behaviour and lacking in the optimisation of the material surface. However, this study demonstrates that promising results have been obtained using an economic and scalable approach, and improvements are expected with material engineering for the specific  $\text{N}_2$  fixation reaction.

## Experimental

### Synthesis of LDHs

LDH samples were all synthesised using a co-precipitation method. In general, metal nitrates were dissolved in water to form a 1.1 M solution (solution A), according to the procedure described by Wu *et al.*<sup>66</sup> Solution A was then added dropwise to 50 mL of 0.2 M  $\text{NaNO}_3$  solution in a 60 °C water bath, while constant pH was achieved by addition of 0.9 M NaOH solution. Suitable pH values have to be chosen for each sample. As well as providing good control over the stability during synthesis, the correct pH is essential to obtain the desired material; indeed, the undesired precipitation of metal hydroxides as  $\text{Al(OH)}_3$  or  $\text{Cu(OH)}_2$  could lead to the formation of impurities in the final catalyst. For this reason, Pourbaix diagrams were used to choose the reaction environment, finding the optimal pH values for Al- and Cr-based LDHs to be 8 and 10, respectively;<sup>67</sup> a summary of the reaction conditions is presented in Table 4. An aging step was then performed at 80 °C for 24 h while constantly stirring the solution. The slurry was filtered and thoroughly washed with deionized water three times. Subsequently, the clay was dried at 100 °C for 24 h.

**Table 4** Tabular summary of the synthesised materials. From the left, the name of each compound, the ratio between the metallic species and the pH of precipitation chosen

Sample name	Cation ratio	Co-precipitation conditions
CuCr	Cu : Cr = 1 : 1	pH = 10
CuAl	Cu : Al = 1 : 1	pH = 8
CuNiCr	Cu : Ni : Cr = 1 : 1 : 2	pH = 10
CuNiAl	Cu : Ni : Al = 1 : 1 : 2	pH = 8



## Catalyst characterisation

XRD measurements were performed using a Bruker D8 ADVANCE diffractometer with a Bragg–Brentano geometry and using Cu K $\alpha$  radiation ( $\lambda = 0.1548$  nm). Diffractograms were collected with  $2\theta$  ranging from  $5^\circ$  to  $75^\circ$ , and with rates of  $0.035^\circ$  per step and 1 s per step, while 40 kV and 40 mA were set as the working conditions. Scanning electron microscopy (SEM) was carried out using a Zeiss Supra 40VP. Specific surface area (SSA) evaluation was possible by means of a Micromeritics ASAP 2020 Plus. The samples were loaded in a quartz reactor and degassed at  $200^\circ\text{C}$  for 16 h; subsequently, N<sub>2</sub>-sorption curves were obtained at liquid nitrogen temperature ( $T = 77$  K) in order to evaluate the SSA from the BET equation. Temperature programmed reduction (TPR) measurements were performed using an AutoChem II 2920 Micromeritics coupled with a TCD detector and using a quartz tube reactor loaded with 50 mg of the sample. TPR measurements were carried out after outgassing the samples with He at  $50\text{ mL min}^{-1}$  and subsequently heating from RT to  $900^\circ\text{C}$  at  $10^\circ\text{C min}^{-1}$  in a 5% H<sub>2</sub>/Ar atmosphere.

## Catalytic tests

To understand the behaviour of each catalyst in the production of ammonia, catalytic tests were performed. 50 mg of the synthesised material was dispersed in 100 mL of water. The suspension was stirred for 1 h at reflux under N<sub>2</sub> at room temperature to effectively ensure equilibrium conditions and good homogeneity in the solution. Subsequently, the system was sealed, and a 100 W LED lamp (BridgeLux BXRC-40A10K1-B-73) was turned on for 1 h to illuminate the catalyst. To evaluate the ammonia production, a spectrophotometric procedure was employed, as the concentration of the reaction product was proven to be below the detection limits of common titration methods. After the catalytic test, the catalyst was removed by filtration; 50 mL of the filtered solution was then mixed with 2 drops of a potassium sodium tartrate solution and with 1 mL of Nessler's reagent. Finally, the solution was analysed using a Shimadzu-1601 spectrophotometer, using distilled water as the reference, and analysing the reaction product solution with a 400 nm wavelength.

## Conclusions

In this work, various types of layered double hydroxides were evaluated as novel catalysts for photo-assisted dinitrogen fixation. Firstly, the reported synthetic method resulted in an effective, scalable, and economical way to produce these types of catalysts; the structures obtained are comparable with similar materials synthesised with different methodologies, thus confirming the validity of the process. In particular, XRD patterns revealed that the copper–aluminium LDH has a different structure compared with the other samples, probably due to a preferential exposition of different facets. SEM images showed that the same material has a different morphology, characterised by a plate-like structure, while the other LDHs present aggregates formed by little particles, with signs of delamination, particularly for CuCr. Temperature programmed reduction analysis pointed out the increased reducibility of Cr-based LDHs with respect to the Al-based counterpart, as well as a stabilization effect of Ni in both types of structure. BET measurements resulted in observing a high surface area and small pore size for CuNiAl, suggesting a weaker interaction between the nanosheets,



causing the formation of small open pores, and thus improving the SSA. From the evaluation of the catalytic performances of these materials, a  $\text{NH}_3$  production rate of  $99 \text{ }\mu\text{mol g}^{-1} \text{ h}^{-1}$  was achieved for CuNiAl using a commercial 100 W visible-light LED lamp; interestingly, the CuAl sample performed the worst, probably due to an inefficient facet exposition. Moreover, the low surface area of CuNiCr, compared with that of CuNiAl, caused a lower active site concentration and, therefore, a worsening of the performance. Comparing the CuCr and CuNiCr samples, it can be noted that nickel insertion resulted in better activity, probably due to the creation of defects and to the modulation of the electronic structure. Deeper studies are needed to confirm the role of Ni in  $\text{N}_2$  activation and the relationship between the facet exposition and the catalytic performances.

## Conflicts of interest

There are no conflicts to declare.

## Acknowledgements

The authors thanks PARTIAL-PGM (H2020) and KNOWSKITE-X (HE) for funding. A special thanks goes to Dr Annalisa Sandon for the  $\text{NH}_3$  detection tests.

## Notes and references

- 1 J. W. Erisman, M. A. Sutton, J. Galloway, Z. Klimont and W. Winiwarter, *Nat. Geosci.*, 2008, **1**(10), 636–639.
- 2 J. N. Galloway, F. J. Dentener, D. G. Capone, E. W. Boyer, R. W. Howarth, S. P. Seitzinger, G. P. Asner, C. C. Cleveland, P. A. Green, E. A. Holland, D. M. Karl, A. F. Michaels, J. H. Porter, A. R. Townsend and C. J. Vörösmarty, *Biogeochemistry*, 2004, **70**, 153–226.
- 3 W. M. Stewart, D. W. Dibb, A. E. Johnston and T. J. Smyth, *Agron. J.*, 2005, **97**, 1–6.
- 4 J. Guo and P. Chen, *Chem.*, 2017, **3**, 709–712.
- 5 M. Benés, G. Pozo, M. Abián, Á. Millera, R. Bilbao and M. U. Alzueta, *Energy Fuels*, 2021, **35**, 7193–7200.
- 6 J. Humphreys, R. Lan and S. Tao, *Adv. Energy Sustain. Res.*, 2021, **2**, 2000043.
- 7 J. S. Anderson, J. Rittle and J. C. Peters, *Nature*, 2013, **501**(7465), 84–87.
- 8 V. Kyriakou, I. Garagounis, A. Vourros, E. Vasileiou and M. Stoukides, *Joule*, 2020, **4**, 142–158.
- 9 T. Kandemir, M. E. Schuster, A. Senyshyn, M. Behrens and R. Schlögl, *Angew. Chem., Int. Ed.*, 2013, **52**, 12723–12726.
- 10 S. Ajmal, A. Rasheed, N. Q. Tran, X. Shao, Y. Hwang, V. Q. Bui, Y. D. Kim, J. Kim and H. Lee, *Appl. Catal., B*, 2023, **321**, 122070.
- 11 C. J. M. van der Ham, M. T. M. Koper and D. G. H. Hetterscheid, *Chem. Soc. Rev.*, 2014, **43**, 5183–5191.
- 12 A. Chen and B. Y. Xia, *J. Mater. Chem. A*, 2019, **7**, 23416–23431.
- 13 Z. Yan, M. Ji, J. Xia and H. Zhu, *Adv. Energy Mater.*, 2020, **10**, 1902020.
- 14 X. Chen, N. Li, Z. Kong, W. J. Ong and X. Zhao, *Mater. Horiz.*, 2018, **5**, 9–27.
- 15 M. P. Shaver and M. D. Fryzuk, *Adv. Synth. Catal.*, 2003, **345**, 1061–1076.
- 16 A. R. Singh, J. H. Montoya, B. A. Rohr, C. Tsai, A. Vojvodic and J. K. Nørskov, *ACS Catal.*, 2018, **8**, 4017–4024.



17 Y. Fu, Y. Liao, P. Li, H. Li, S. Jiang, H. Huang, W. Sun, T. Li, H. Yu, K. Li, H. Li, B. Jia and T. Ma, *Coord. Chem. Rev.*, 2022, **460**, 214468.

18 L. Hao, H. Huang, Y. Zhang and T. Ma, *Adv. Funct. Mater.*, 2021, **31**, 25.

19 Y. Yang, M. Wu, X. Zhu, H. Xu, S. Ma, Y. Zhi, H. Xia, X. Liu, J. Pan, J. Y. Tang, S. P. Chai, L. Palmisano, F. Parrino, J. Liu, J. Ma, Z. L. Wang, L. Tan, Y. F. Zhao, Y. F. Song, P. Singh, P. Raizada, D. Jiang, D. Li, R. A. Geioushy, J. Ma, J. Zhang, S. Hu, R. Feng, G. Liu, M. Liu, Z. Li, M. Shao, N. Li, J. Peng, W. J. Ong, N. Kornienko, Z. Xing, X. Fan and J. Ma, *Chin. Chem. Lett.*, 2019, **30**, 2065–2088.

20 G. Marnellos and M. Stoukides, *Science*, 1998, **282**, 98–100.

21 S. Zhang, Y. Zhao, R. Shi, C. Zhou, G. I. N. Waterhouse, L. Z. Wu, C. H. Tung and T. Zhang, *Adv. Energy Mater.*, 2020, **10**(8), DOI: [10.1002/aenm.201901973](https://doi.org/10.1002/aenm.201901973).

22 Y. Zhao, Y. Zhao, G. I. N. Waterhouse, L. Zheng, X. Cao, F. Teng, L. Z. Wu, C. H. Tung, D. O'Hare and T. Zhang, *Adv. Mater.*, 2017, **29**(42), DOI: [10.1002/adma.201703828](https://doi.org/10.1002/adma.201703828).

23 K. Ithisuphalap, H. Zhang, L. Guo, Q. Yang, H. Yang and G. Wu, *Small Methods*, 2019, **3**, 1800352.

24 H. D. Vandervell and K. C. Waugh, *Chem. Phys. Lett.*, 1990, **171**, 462–468.

25 N. Usberti, M. Jablonska, M. di Blasi, P. Forzatti, L. Lietti and A. Beretta, *Appl. Catal., B*, 2015, **179**, 185–195.

26 W. Shan, Y. Yu, Y. Zhang, G. He, Y. Peng, J. Li and H. He, *Catal. Today*, 2021, **376**, 292–301.

27 I. J. McPherson, T. Sudmeier, J. Fellowes and S. C. E. Tsang, *Dalton Trans.*, 2019, **48**, 1562–1568.

28 Q. Liu, T. Xu, Y. Luo, Q. Kong, T. Li, S. Lu, A. A. Alshehri, K. A. Alzahrani and X. Sun, *Curr. Opin. Electrochem.*, 2021, **29**, 100766.

29 Y. Zhao, R. Shi, X. Bian, C. Zhou, Y. Zhao, S. Zhang, F. Wu, G. I. N Waterhouse, L.-Z. Wu, C.-H. Tung, T. Zhang, Y. X. Zhao, R. Shi, X. A. Bian, C. Zhou, Y. F. Zhao, S. Zhang, F. Wu, L. Wu, C. Tung, T. R. Zhang and G. I. N Waterhouse, *Adv. Sci.*, 2019, **6**, 1802109.

30 M. Hölscher and W. Leitner, *Chem. – Eur. J.*, 2017, **23**, 11992–12003.

31 E. Cortés, L. v. Besteiro, A. Alabastri, A. Baldi, G. Tagliabue, A. Demetriadou and P. Narang, *ACS Nano*, 2020, **14**, 16202–16219.

32 G. Centi and S. Perathoner, *Microporous Mesoporous Mater.*, 2008, **107**, 3–15.

33 Y. Wang, B. Ren, J. Zhen Ou, K. Xu, C. Yang, Y. Li and H. Zhang, *Sci. Bull.*, 2021, **66**, 1228–1252.

34 S. Ajmal, A. Rasheed, N. Q. Tran, X. Shao, Y. Hwang, V. Q. Bui, Y. D. Kim, J. Kim and H. Lee, *Appl. Catal., B*, 2023, **321**, 122070.

35 L. Zhang, W. Zhao, W. Zhang, J. Chen and Z. Hu, *Nano Res.*, 2019, **12**(5), 1181–1186.

36 L. M. Azofra, N. Li, D. R. Macfarlane and C. Sun, *Energy Environ. Sci.*, 2016, **9**, 2545–2549.

37 J. D. Gouveia, Á. Morales-García, F. Viñes, J. R. B. Gomes and F. Illas, *ACS Catal.*, 2020, **10**, 5049–5056.

38 G. R. Williams and D. O'Hare, *J. Mater. Chem.*, 2006, **16**, 3065–3074.

39 C. Forano, T. Hibino, F. Leroux and C. Taviot-Guého, *Dev. Clay Sci.*, 2006, **1**, 1021–1095.

40 S. He, Z. An, M. Wei, D. G. Evans and X. Duan, *Chem. Commun.*, 2013, **49**, 5912–5920.



41 S. Podila, H. Driss, S. F. Zaman, A. M. Ali, A. A. Al-Zahrani, M. A. Daous and L. A. Petrov, *Int. J. Hydrogen Energy*, 2020, **45**, 873–890.

42 P. Zang, J. Liu, Y. He, G. Zhang, G. Li, Y. Wang and Y. Lv, *Chem. Eng. J.*, 2022, **446**, 137414.

43 G. Carja and G. Delahay, *Appl. Catal., B*, 2004, **47**, 59–66.

44 J. Li, G. Zhang, S. Han, J. Cao, L. Duan and T. Zeng, *Chem. Commun.*, 2018, **54**, 723–726.

45 I. Kim, S. So, A. S. Rana, M. Q. Mehmood and J. Rho, *Nanophotonics*, 2018, **7**, 1827–1833.

46 J. M. Igual, C. Rodríguez-Barrueco and E. Cervantes, *Plant Soil*, 1997, **190**(1), 41–46.

47 J. D. Egbert, M. O'Hagan, E. S. Wiedner, R. M. Bullock, N. A. Piro, W. S. Kassel and M. T. Mock, *Chem. Commun.*, 2016, **52**, 9343–9346.

48 M. H. Vu, M. Sakar and T. O. Do, *Catalysts*, 2018, **8**, 621.

49 Z. Xiao, X. Wang, J. Xiu, Y. Wang, C. T. Williams and C. Liang, *Catal. Today*, 2014, **234**, 200–207.

50 M. Lv and H. Liu, *J. Solid State Chem.*, 2015, **227**, 232–238.

51 L. Wu, X. Zhou, G. Wan, Y. Tang, S. Shi, X. Xu and G. Wang, *Dalton Trans.*, 2021, **50**, 95–102.

52 X. Wu, H. Meng, Y. Du, J. Liu, B. Hou and X. Xie, *ACS Appl. Mater. Interfaces*, 2019, **11**, 32917–32927.

53 A. S. Patil, J. L. Gunjakar, C. D. Lokhande, U. M. Patil, S. v. Sadavar, N. S. Padalkar, R. B. Shinde, M. M. Wagh and J. S. Bagi, *Synth. Met.*, 2020, **264**, 116371.

54 A. L. Boyce, S. R. Graville, P. A. Sermon and M. S. W. Vong, *React. Kinet. Catal. Lett.*, 1991, **44**(1), 13–18.

55 A. Ebadi, J. S. Soltan Mohammadzadeh and A. Khudiev, *Adsorption*, 2009, **15**(1), 65–73.

56 D. Bharali, R. Devi, P. Bharali and R. C. Deka, *New J. Chem.*, 2015, **39**, 172–178.

57 A. L. Boyce, S. R. Graville, P. A. Sermon and M. S. W. Vong, *React. Kinet. Catal. Lett.*, 1991, **44**(1), 1–11.

58 S. Tanasoi, N. Tanchoux, A. Urdă, D. Tichit, I. Săndulescu, F. Fajula and I. C. Marcu, *Appl. Catal., A*, 2009, **363**, 135–142.

59 H. Lee, A. Hong, J. Kwak and S. Lee, *RSC Adv.*, 2022, **12**, 4322–4328.

60 M. Qi, L. Fan, Y. Shen, H. Zou, X. Tian, D. Liu and S. Li, *J. Nanosci. Nanotechnol.*, 2018, **18**, 753–760.

61 Y. Gorbanev, Y. Engelmann, K. Van'T Veer, E. Vlasov, C. Ndayirinde, Y. Yi, S. Bals and A. Bogaerts, *Catalysts*, 2021, **11**, 1230.

62 Y. Zhao, L. Zheng, R. Shi, S. Zhang, X. Bian, F. Wu, X. Cao, G. I. N Waterhouse, T. Zhang, Y. Zhao, R. Shi, S. Zhang, X. Bian, F. Wu, T. Zhang, L. Zheng, X. Cao and G. I. N Waterhouse, *Adv. Energy Mater.*, 2020, **10**, 2002199.

63 Y. Zhao, Y. Zhao, R. Shi, B. Wang, G. I. N. Waterhouse, L. Z. Wu, C. H. Tung and T. Zhang, *Adv. Mater.*, 2019, **31**, 1806482.

64 J. Yang, Y. Guo, R. Jiang, F. Qin, H. Zhang, W. Lu, J. Wang and J. C. Yu, *J. Am. Chem. Soc.*, 2018, **140**, 8497–8508.

65 G. Dong, W. Ho and C. Wang, *J. Mater. Chem. A*, 2015, **3**, 23435–23441.

66 Q. Wu, A. Olafsen, Ø. B. Vistad, J. Roots and P. Norby, *J. Mater. Chem.*, 2005, **15**, 4695–4700.

67 E. McCafferty, *Introduction to Corrosion Science*, 2010, pp. 95–117.

